On the Propagation of Concentration Polarization from Microchannel−Nanochannel Interfaces Part I: Analytical Model and Characteristic Analysis

Ali Mani, Thomas A. Zangle, and Juan G. Santiago*

Department of Mechanical Engineering, Stanford University, Stanford, California 94305

Received October 8, 2008. Revised Manuscript Received December 7, 2008

We develop two models to describe ion transport in variable-height micro- and nanochannels. For the first model, we obtain a one-dimensional (unsteady) partial differential equation governing flow and charge transport through a shallow and wide electrokinetic channel. In this model, the effects of electric double layer (EDL) on axial transport are taken into account using exact solutions of the Poisson−Boltzmann equation. The second simpler model, which is approachable analytically, assumes that the EDLs are confined to near-wall regions. Using a characteristics analysis, we show that the latter model captures concentration polarization (CP) effects and provides useful insight into its dynamics. Two distinct CP regimes are identified: CP with propagation in which enrichment and depletion shocks propagate outward, and CP without propagation where polarization effects stay local to micro- nanochannel interfaces. The existence of each regime is found to depend on a nanochannel Dukhin number and mobility of the co-ion nondimensionalized by electroosmotic mobility. Interestingly, microchannel dimensions and axial diffusion are found to play an insignificant role in determining whether CP propagates. The steady state condition of propagating CP is shown to be controlled by channel heights, surface chemistry, and co-ion mobility instead of the reservoir condition. Both models are validated against experimental results in Part II of this two-paper series.

Introduction

Recent advances in fabrication technology[1−5] have enabled nanofluidic devices with long, thin channels (with characteristic dimensions of 10−100 nm) to be leveraged for sample analysis[5−11] and preparation.[12,13] Nanofluidic devices exploit length scales on the order of biomolecule sizes[14,15] or the thickness of electrical double layers (EDLs). Pennathur and Santiago,[3,4] and Griffiths and Nilson[7] showed that long thin nanochannels can be used for separation on the basis of ion valence as well as mobility. Tegenfeldt et al.[2] and Pennathur et al.[11] reported unique features of DNA migration through a nanochannel device. Schoch et al.[16] demonstrated the use of a nanochannel as a sensor for antibody−antigen binding. Finally, Han et al.[9] reviewed the use of nanofluidic devices for molecular sieving. Combining the properties of nanofluidics with microfluidic systems requires an understanding of the interface between microchannels and nanofluidic devices.

Complex behaviors emerge from the integration of electrokinetic nano- and microchannels.[12,17−24] One primary phenomenon is concentration polarization[25,26] (CP) which Pu et al.[19] observed at a microchannel−nanochannel interface and described with qualitative models. CP has also long been studied in the context of electrokinetic transport through membrane systems[27−29] which can be used for a qualitative understanding of CP in micro- and nanochannels.[19] The conventional description of CP shows enrichment and depletion regions with molecular diffusion boundary layers which can limit ionic fluxes and current.[30,31] Rubenstein and Zaltzman[32] developed a model of electroconvective instability and its role in overlimiting current. In Part II of this two-paper series, we review experimental observations of CP in microfluidic systems.

Recent studies have shown that the bulk flow effects are critical in capturing the effects of CP.[23,33−35] To our knowledge, Zangle et al.'s conference paper[36] was the first describing the coupling of CP with bulk flow and the existence of ion concentration shocks emerging from CP zones. Despite these descriptions, important questions remain regarding the nature of and factors determining the propagation of CP.

* To whom correspondence should be addressed. Mailing address: 440 Escondido Mall, Bldg. 530, room 225, Stanford, CA 94305. E-mail: juan.santiago@stanford.edu. Fax: (650) 723-7657.

(1) Hibara, A.; Saito, T.; Kim, H.-B.; Tokeshi, M.; Ooi, T.; Nakao, M.; Kitamori, T. *Anal. Chem.* **2002**, *74*, 6170–6176.
(2) Tegenfeldt, J. O.; Prinz, C.; Cao, H.; Huang, R. L.; Austin, R. H.; Chou, S. Y.; Cox, E. C.; Sturm, J. C. *Anal. Bioanal. Chem.* **2004**, *378*, 1678–1692.
(3) Pennathur, S.; Santiago, J. G. *Anal. Chem.* **2005**, *77*, 6772–6781.
(4) Pennathur, S.; Santiago, J. G. *Anal. Chem.* **2005**, *77*, 6782–6789.
(5) Garcia, A. L.; Ista, L. K.; Petsev, D. N.; O'Brien, M. J.; Bisong, P.; Mammoli, A. A.; Brueck, S. R. J.; Lopez, G. P. *Lab Chip* **2005**, *5*, 1271–1276.
(6) Eijkel, J. C. T.; van den Berg, A. *Microfluid. Nanofluid.* **2005**, *1*, 249–267.
(7) Griffiths, S. K.; Nilson, R. H. *Anal. Chem.* **2006**, *78*, 8134–8141.
(8) Wang, K.-G.; Yue, S.; Wang, L.; Jin, A.; Gu, C.; Wang, P.-Y.; Feng, Y.; Wang, Y.; Niu, H. *Microfluid. Nanofluid.* **2006**, *2*, 85–88.
(9) Han, J.; Fu, J.; Schoch, R. B. *Lab Chip* **2008**, *8*, 23–33.
(10) Mannion, J. T.; Craighead, H. G. *Biopolymers* **2006**, *85*, 131–143.
(11) Pennathur, S.; Baldessari, F.; Santiago, J. G.; Kattah, M. G.; Steinmen, J. B.; Utz, P. J. *Anal. Chem.* **2007**, *79*, 8316–8322.
(12) Wang, Y.-C.; Stevens, A. L.; Han, J. *Anal. Chem.* **2005**, *77*, 4293–4299.
(13) Song, S.; Singh, A. K. *Anal. Bioanal. Chem.* **2006**, *384*, 41–43.
(14) Sexton, L. T.; Horne, L. P.; Sherrill, S. A.; Bishop, G. W.; Baker, L. A.; Martin, C. R. *J. Am. Chem. Soc.* **2007**, *129*, 13144–13152.
(15) Gauthier, M. G.; Slater, G. W. *J. Chem. Phys.* **2008**, *128*, 065103.
(16) Schoch, R. B.; Cheow, L. F.; Han, J. *Nano Lett.* **2007**, *7*, 3895–3900.
(17) Höltzel, A.; Tallarek, U. *J. Sep. Sci.* **2007**, *30*, 1398–1419.
(18) Park, S. Y.; Russo, C. J.; Branton, D.; Stone, H. A. *J. Colloid Interface Sci.* **2006**, *297*, 832–839.
(19) Pu, Q.; Yun, J.; Temkin, H.; Liu, S. *Nano Lett.* **2004**, *4*, 1099–1103.
(20) Plecis, A.; Schoch, R. B.; Renaud, P. *Nano Lett.* **2005**, *5*, 1147–1155.
(21) Schoch, R. B.; van Lintel, H.; Renaud, P. *Phys. Fluids* **2005**, *17*, 100604.
(22) Schoch, R. B.; Bertsch, A.; Renaud, P. *Nano Lett.* **2006**, *6*, 543–547.
(23) Kim, S. J.; Wang, Y.-C.; Lee, J. H.; Jang, H.; Han, J. *Phys. Rev. Lett.* **2007**, *99*, 044501.
(24) Ramirez, J. C.; Conlisk, A. T. *Biomed. Microdevices* **2006**, *8*, 325–330.
(25) Mishchuk, N. A.; Takhistov, P. V. *Colloids Surf., A* **1995**, *95*, 119–131.
(26) Dukhin, S. S.; Shilov, V. N. *Kolloidn. Zh.* **1969**, *31*, 706–713.
(27) Probstein, R. F. *Physicochemical Hydrodynamics: An Introduction*, 2nd ed.; John Wiley & Sons, Inc.: New York, 2003.
(28) Horno, J.; Gonzalez-Fernandez, C. F.; Hayas, A.; Gonzalez-Caballero, F. *Biophys. J.* **1989**, *55*, 527–535.
(29) Rubinstein, I.; Zaltzman, B. *Phys. Rev. E* **2000**, *62*, 2238–2251.
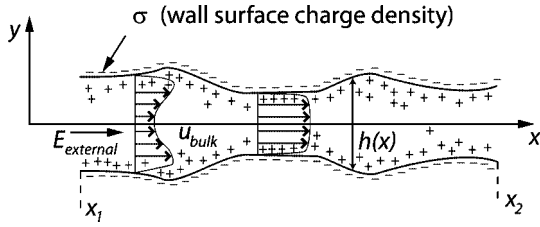(30) Leinweber, F. C.; Tallarek, U. *Langmuir* **2004**, *20*, 11637–11648.

Figure 1. Schematic of an arbitrary variable height channel. Our model includes advection due to electroosmosis and internal pressure gradients, electromigration, and diffusion of bulk and electric double layer ions. External electric field and bulk flow profiles are shown. The model allows for either known volume flow rate or known end pressures at locations x_1 and x_2. The model also uses either a specified current or a specified voltage drop. Relatively large regions have adverse pressure gradients, while smaller nanochannel regions have favorable pressure gradients (which are typically small relative to the local electroosmotic flow).

In this paper, we present a transport model for CP in fairly arbitrary channel geometries, which includes the coupling of CP with electroosmotic and pressure-driven flow. Our model predicts ion transport in channels with either nonoverlapped or overlapped EDLs using nanochannel wall charge as the only fitting parameter. In Part II of this two-paper series,[37] we use this model to study a series microchannel−nanochannel−microchannel geometry where we examine the spatial and temporal evolution of CP in comparison to experiments. We identify two possible CP regimes: one where polarization effects remain local to channel interfaces (CP without propagation), and another where concentration shock waves are transmitted from these interfaces (CP with propagation). Using a simplified, analytically approachable version of the model, we identify major system parameters and their coupling with CP. Analysis based on the method of characteristics yields important new insights into the physics of CP including conditions for the existence and propagation of CP, and asymptotic behavior of the system.

Area-Averaged Model

We here derive a one-dimensional partial differential equation (PDE) for transport of ionic species in a channel

system with variable height. We also present a solution algorithm. Transport of ions in a dilute solution is described by the following equation:

$$\frac{\partial}{\partial t}c_i + \nabla\cdot(\vec{u}c_i + \nu_i z_i F\vec{E}c_i) = D_i\nabla^2 c_i \quad (1)$$

where c_i, ν_i, z_i, and D_i represent concentration, mobility, valence number, and diffusion coefficient of the ith ion, respectively (see Table 1). $\vec{u}$ and $\vec{E}$ are the velocity and electric fields, respectively, and F is the Faraday number. We consider two dominant ionic species with subscripts 1 and 2 for positive and negative species, respectively. We use Cartesian coordinates to describe a channel with height $h(x)$ (see Figure 1). Consistent with the experiments, we will present in Part II, we assume the channel width (into the paper) is much larger than the maximum value of $h(x)$.

To obtain one-dimensional transport equations, we integrate eq 1 in the y direction. Given the zero-flux condition at the walls, these can be represented in the following form:

$$\frac{\partial}{\partial t}(h\bar{c}_1) + \frac{\partial}{\partial x}(h\overline{u^{\text{p}}}\tilde{c}_1^{\text{p}} + h\overline{u^{\text{e}}}\tilde{c}_1^{\text{e}} + \nu_1 z_1 FhE\bar{c}_1) = \frac{\partial}{\partial x}\left[hD_1\overline{\frac{\partial c_1}{\partial x}}\right] \quad (2)$$

$$\frac{\partial}{\partial t}(h\bar{c}_2) + \frac{\partial}{\partial x}(h\overline{u^{\text{p}}}\tilde{c}_2^{\text{p}} + h\overline{u^{\text{e}}}\tilde{c}_2^{\text{e}} + \nu_2 z_2 FhE\bar{c}_2) = \frac{\partial}{\partial x}\left[hD_2\overline{\frac{\partial c_2}{\partial x}}\right] \quad (3)$$

where superscripts e and p stand for electroosmotic and pressure-driven velocity components, respectively. The overbar symbol represents the height average operator, and the tilde is a velocity-weighted height average so that

$$\bar{c}_i = \frac{1}{h}\int_{-h/2}^{h/2} c_i\,\mathrm{d}y, \quad \bar{u} = \frac{1}{h}\int_{-h/2}^{h/2} u\,\mathrm{d}y,$$

$$\tilde{c}_i^{\text{p}} = \frac{1}{h\overline{u^{\text{p}}}}\int_{-h/2}^{h/2} u^{\text{p}}c_i\,\mathrm{d}y, \quad \tilde{c}_i^{\text{e}} = \frac{1}{h\overline{u^{\text{e}}}}\int_{-h/2}^{h/2} u^{\text{e}}c_i\,\mathrm{d}y \quad (4)$$

For wide channels, area-averaged quantities for mass, momentum, and species transport are well approximated by averages over

Table 1. Nomenclature

parameter	description	parameter	description
c_i	concentration of the ith ion	u_0^{e}	electroosmotic velocity away from wall
c_0	concentration of the counterion away from wall[a]	U^*	dimensionless characteristic velocity
c_{n}^*	dimensionless c_0 in the nanochannel	U_{n}^*	dimensionless characteristic velocity in the nanochannel
c_{r}^*	dimensionless c_0 in the reservoir	V^*	dimensionless shock velocity
D_i	diffusion coefficient of the ith ion	V_1^*	dimensionless shock velocity in the depletion zone
E	axial electric field	z_i	valence number of the ith ion
F	Faraday number	ε	permittivity
$f, f^{\text{e}}, f_1^{\text{p}}, f_2^{\text{p}}, f_1^{\text{e}}, f_{\text{e}}^2$	integral factors (functions of σ^*, λ^*, z_2/z_1)	η	viscosity
f^ζ	dimensionless zeta potential (function of σ^*, λ^*, z_2/z_1)	e	charge of proton
h	channel height	λ	Debye length
h_{n}^*	dimensionless nanochannel height	ν_i	mobility of the ith ion
I	current per width	ν_2^*	dimensionless mobility of the coion
Q	volume flow rate per width	$\nu_{2\text{n}}^*$	dimensionless mobility of the coion in the nanochannel
u	axial velocity	σ	wall charge
u^{p}	axial pressure-driven velocity	ψ	wall normal potential
u^{e}	axial electroosmotic velocity	ζ	zeta potential

superscript	description	subscript	description
*	dimensionless quantity	i	arbitrary species i
e	associated with electroosmotic flow velocity	1	counterion
p	associated with pressure-driven flow	2	co-ion
−	standard area-average	1, 2, 3, 4, 5	micro−nano−microchannel regions
∼e	area-averaged (weighted by electroosmotic velocity)	0	associated with away from EDL (bulk)
∼p	area-averaged (weighted by pressure-driven velocity)	n	associated with nanochannel

[a] Mathematically defined as the Poisson−Boltzmann distribution constant (i.e., the prefactor to the exponential of scaled electric potential).
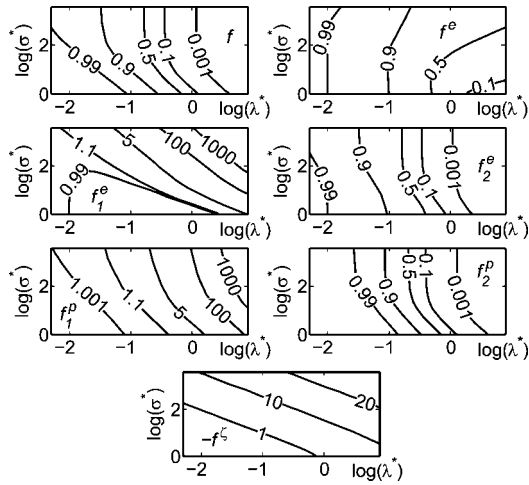
Figure 2. Contour plots of integral factors introduced in the area-averaged model for valence ratio $z_2/z_1 = -2$ and as a function of σ^* and λ^*. λ^* is the ratio of the local Debye length (based on c_0) to the local channel half-height, and σ^* is the electric field associated with the local wall surface charge density nondimensionalized by the local channel half-width and thermal voltage (see eq 8). Under our local equilibrium assumption, these factors are obtained from numerical solutions of the Poisson–Boltzmann equation integrated in the wall normal direction.

the shallow dimension (height). Therefore, these integrals can be interpreted as cross-sectional, area-averaged quantities. Equations 2 and 3 are exact representations of the transport of ionic species in terms of height-averaged quantities. However, to bring closure to these equations we use the following approximations:

1. At each section of the channel, the effect of wall slope on concentrations and axial fields can be neglected (similar to the lubrication theory assumption[38]).
2. To simplify our results, we approximate streamwise diffusion fluxes with simple terms that capture only the order of magnitude of diffusive effects.
3. We assume that diffusion and electromigration in the y direction are in equilibrium. In other words, the time scale governing EDL is much smaller than that of axial transport.

Under these conditions, at each section of the channel, parametrized Poisson–Boltzmann equations can describe the wall normal potential and distribution of the ionic species.[39] These equations can be presented in the following nondimensional form:

$$\frac{c_1}{c_0} = \exp\left(\frac{-2}{1 - z_2/z_1}\psi^*\right), \quad \frac{c_2}{c_0} = \left(\frac{z_1}{-z_2}\right)\exp\left(\frac{-2z_2/z_1}{1 - z_2/z_1}\psi^*\right) \tag{5}$$

$$\frac{d^2\psi^*}{dy^{*2}} = -\frac{1}{2\lambda^{*2}}\left[\exp\left(\frac{-2}{1 - z_2/z_1}\psi^*\right) - \exp\left(\frac{-2z_2/z_1}{1 - z_2/z_1}\psi^*\right)\right] \tag{6}$$

(31) Postler, T.; Slouka, Z.; Svoboda, M.; Přibyl, M.; Šnita, D. *J. Colloid Interface Sci.* **2008**, *320*, 321–332.
(32) Zaltzman, B.; Rubinstein, I. *J. Fluid Mech.* **2007**, *579*, 173–226.
(33) Ehlert, S.; Hlushkou, D.; Tallarek, U. *Microfluid. Nanofluid.* **2007**, .
(34) Dhopeshwarkar, R.; Crooks, R. M.; Hlushkou, D.; Tallarek, U. *Anal. Chem.* **2008**, *80*, 1039–1048.
(35) Jin, X.; Joseph, S.; Gatimu, E. N.; Bohn, P. W.; Aluru, N. R. *Langmuir* **2007**, *23*, 13209–13222.
(36) Zangle, T. A.; Mani, A.; Santiago, J. G. *Novel Device for Electrophoretic Focusing and Separation at a Microchannel-Nanochannel Interface*, Proceedings of μTAS 2007, Paris, France, October 7–11, 2007; Viovy, J. L., Tabeling, P., Descroix, S., Malaquin, L., Eds.; Chemical and Biological Microsystems Society: San Diego, CA, 2007; Vol. 2, pp 1204–1206.
(37) Zangle, T. A.; Mani, A.; Santiago, J. G. *Langmuir* **2009**, *25*, 3909-3916.

$$\left.\frac{d\psi^*}{dy^*}\right|_{y^*=\pm 1} = -\sigma^* \tag{7}$$

where ψ^* is the electric potential generated by the surface charge nondimensionalized by the thermal voltage, $2kT/e(z_1-z_2)$ (k, T, and e are the Boltzmann constant, temperature, and charge of proton, respectively), and y^* is the wall normal coordinate nondimensionalized by the local channel half-height. c_0, which varies in x, is the Boltzmann distribution constant and mathematically represents the ion concentration where ψ^* is zero. We note that c_0 is not the channel centerline concentration if EDLs overlap. The centerline concentration will be $c_0 \exp(-z_i e\psi|_{y=0}/kT)$, where $\psi|_{y=0}$ is (a function of x and) obtained after solving the Poisson–Boltzmann equation subject to the two boundary conditions at the walls (eq 7). λ^* and σ^* are the nondimensional Debye length and wall charge, respectively:

$$\lambda^* = \frac{2}{h}\sqrt{\frac{\varepsilon kT}{e(z_1 - z_2)Fc_0 z_1}}, \quad \sigma^* = \frac{\sigma he(z_1 - z_2)}{4\varepsilon kT} \tag{8}$$

where ε is the permittivity of the electrolyte. The only nondimensional parameters of this Poisson–Boltzmann problem are z_2/z_1, λ^*, and σ^*. From eqs 5–7, we see that

$$\bar{c}_2 = c_0(-z_1/z_2)\,f(z_2/z_1, \lambda^*, \sigma^*). \tag{9}$$

The function f can be obtained by numerically solving eqs 6 and 7 (see Figure 2). These solutions can be tabulated for use with our solution algorithm. Note that λ^* varies with c_0 and we assume that σ is either constant or a function of local c_0. Therefore, from eq 9, $\bar{c}_2$ can be closed in terms of c_0, h, and known physical constants. In general, c_0 varies with x and t, and therefore, to obtain $\bar{c}_2$, we need separate evaluation of f for each section of the channel.

We now describe the procedure for closing other height-averaged quantities. By integrating eq 6 in the y direction and using eqs 5, 7, and 8 we can observe that

$$z_1\bar{c}_1 + z_2\bar{c}_2 + \frac{2\sigma}{hF} = 0 \tag{10}$$

which is an expression of net neutrality and can be used to close $\bar{c}_1$. Using eq 5 and assuming a parabolic pressure-driven velocity profile, $u^p/\overline{u^p} = 3/2(1 - y^*)(1 + y^*)$,[38] one can write in

$$\tilde{c}_1^p = c_0 f_1^p(z_2/z_1, \lambda^*, \sigma^*), \quad \tilde{c}_2^p = c_0(-z_1/z_2)f_2^p(z_2/z_1, \lambda^*, \sigma^*) \tag{11}$$

Similarly, the electroosmotic velocity profile, $u^e = u_0^e(1 - \psi^*/\zeta^*)$,[39] can be used to close $\overline{u^e}$, $\tilde{c}_1^e$, and $\tilde{c}_2^e$.

$$\overline{u^e} = u_0^e f^e(z_2/z_1, \lambda^*, \sigma^*), \quad \tilde{c}_1^e = c_0 \frac{f_1^e(z_2/z_1, \lambda^*, \sigma^*)}{f^e},$$

$$\tilde{c}_2^e = c_0(-z_1/z_2)\frac{f_2^e(z_2/z_1, \lambda^*, \sigma^*)}{f^e} \tag{12}$$

Here, u_0^e is the well-known Helmholtz–Smoluchowski velocity equal to

$$u_0^e = \frac{-\varepsilon\zeta E}{\eta} \tag{13}$$

where η is the viscosity of the solution and ζ is the shear-plane potential ($\zeta^* = \psi_{y^*=\pm 1}^*$). Finally, by using the solution of Poisson–Boltzmann equation at the boundaries, we can see that

$$\zeta = \frac{2kT}{e(z_1 - z_2)} f^{\zeta}(z_2/z_1, \lambda^*, \sigma^*) \tag{14}$$

Now that we closed all of the height-averaged quantities, we rewrite eq 3 in terms of the introduced known functions (*f* factors shown in Figure 2).

$$\frac{\partial}{\partial t}(hf c_0) + \frac{\partial}{\partial x}\left[h\left(\overline{u^p} f_2^p + u_0^e f_2^e + \nu_2 z_2 FEf\right)c_0\right] = \frac{\partial}{\partial x}\left[hD_2 f \frac{\partial c_0}{\partial x}\right] \tag{15}$$

where all of the *f* factors are known functions of local c_0 and h (see Figure 2 and eq 8). Note that the axial diffusion flux is not treated in exact form, since the bar operator and differentiation do not commute for variable height channels. However, the form of eq 15 is consistent with our lubrication flow approximation (i.e., we assume that $|\partial h/\partial x| \ll 1$). This approximation also provides a consistent solution for the electrochemical potential at equilibrium (i.e., zero external field). By repeating the same procedure for the other species, we obtain another equation for the evolution of c_0.

$$\frac{\partial}{\partial t}\left(hf c_0 - \frac{2\sigma}{z_1 F}\right) + \frac{\partial}{\partial x}\left[h\left(\overline{u^p} f_1^p + u_0^e f_1^e + \nu_1 z_1 FEf\right)c_0 - 2\nu_1 E\sigma\right] = \frac{\partial}{\partial x}\left[hD_1 f \frac{\partial c_0}{\partial x} - \frac{2D_1}{z_1 F} \frac{\partial \sigma}{\partial x}\right] \tag{16}$$

Lastly, conservation of mass can be used to determine the pressure-driven flow.

$$\frac{\partial}{\partial x}\left(h\overline{u^p} + hu_0^e f^e\right) = 0 \tag{17}$$

Equations 15, 16, 17 and 13 are in closed form and can be solved for c_0, E, $\overline{u^p}$, and u_0^e. Two integration constants arise through the solution of this system which can be determined by the electrical and mechanical boundary conditions. The mechanical boundary condition can be either a specified pressure difference between the two ends of the channel or a known volume flow rate. The electrical boundary condition can be an applied voltage drop across the channel or an applied electric current through the channel. In both parts I and II of this two-paper series, we assume a zero external pressure difference and constant current condition, consistent with the experiments of Part II. In addition, we assume that c_0 is equal to a known reservoir concentration at the channel ends.

Solution Method. In this section, we show how pressure-driven flow and the electric field can be obtained in terms of closed equation sets.

Integrating eq 17 and rearranging the terms results in

$$\overline{u^p} = (Q - hf^e u_0^e)/h \tag{18}$$

where Q is the volume flow rate per unit width. A pressure gradient equal to $-12\eta\overline{u^p}/h^2$ is required to drive a pressure-driven flow at velocity $\overline{u^p}$.[38] Substituting this relation into eq 18 results in

$$\frac{-1}{12\eta}\frac{\partial p}{\partial x} = \frac{Q - hf^e u_0^e}{h^3} \tag{19}$$

Since the pressure difference between the two ends of the channel is zero, the integral of eq 19 through the channel length should be zero. This leads to the following expression for Q:

$$Q = \int_{x_1}^{x_2}\frac{f^e u_0^e}{h^2}\,dx \Big/ \int_{x_1}^{x_2}\frac{1}{h^3}\,dx \tag{20}$$

Substituting eq 20 into eq 18 results in an explicit expression for $\overline{u^p}$ in terms of u_0^e and together with eq 13 can be substituted

into eqs 15 and 16. By subtracting eq 15 from eq 16, we obtain an expression for conservation of current.

$$\frac{\partial}{\partial t}\left(-\frac{2\sigma}{z_1 F}\right) + \frac{\partial}{\partial x}\left[h\left(\overline{u^p}(f_1^p - f_2^p) + u_0^e(f_1^e - f_2^e) + (\nu_1 z_1 - \nu_2 z_2)FEf\right)c_0 - 2\nu_1 E\sigma\right] = \frac{\partial}{\partial x}\left[h(D_1 - D_2)f\frac{\partial c_0}{\partial x} - \frac{2D_1}{z_1 F}\frac{\partial \sigma}{\partial x}\right] \tag{21}$$

In this model, we include the effect of variations of σ in eq 21 (e.g., with local ion densities) for generality. Nevertheless, for simplicity in the next section and in Part II of this two-paper series, we extensively study a fixed σ model. Furthermore, we ignore the diffusion term in eq 21 (but we keep the diffusion term in eq 15 to capture this effect in an order of magnitude sense). With these simplifications, we can substitute for $\overline{u^p}$ and u_0^e from eqs 18, 20, and 13 and integrate the result in the x direction.

$$\left\{\left[(\nu_1 z_1 - \nu_2 z_2)Ff - \frac{\varepsilon\zeta}{\eta}(f_1^e - f_2^e - f_1^p f^e + f_2^p f^e)\right]hc_0 - 2\nu_1\sigma\right\}E - \frac{\varepsilon(f_1^p - f_2^p)c_0}{\eta\int_{x_1}^{x_2}\frac{dx}{h^3}}\int_{x_1}^{x_2}\frac{f^e\zeta E}{h^2}\,dx = \frac{I}{Fz_1} \tag{22}$$

which is an integral equation and can be solved to obtain E in terms of closed quantities. I is the known current through the system that appears as the integration constant.

In our solution method, we time advance eq 15 after closing expressions of E, u_0^e, and $\overline{u^p}$ in terms of c_0. Namely, we use eqs 22, 13, and 18 (together with eq 20) to close these expressions. Note these equations are simply supplementary equations to eq 15 and not PDEs.

Equation 15 is an unsteady, one-dimensional (along the channel axis) partial differential equation with c_0 as the main dependent variable. Before continuing, we note that our resulting equation is one-dimensional in space but does not neglect effects of the second dimension. We simply integrate the effects of the transverse (wall normal) gradients on area-averaged quantities under the aforementioned assumptions. For example, our solution procedure takes into account the effects of transverse gradients of the electric double layer and velocity field. As an illustrative example, we present in Appendix A a calculation of a two-dimensional velocity field based on the area-averaged model presented here. As shown in the Appendix, the solution fully captures the recirculation regions formed by a particular micro-to-nanochannel transition geometry. We hope to explore such effects in more detail in a future paper.

We followed the general solution method described above in a computational model that we developed to simulate ion transport in a nanochannel in series with two microchannels. We present more details of this numerical solution and numerical results in Part II, where we also compare these to experimental measurements.

Simple Model

In this section, we will consider a simplified version of the area-averaged model. This model can be solved analytically and used to qualitatively describe the behavior of the system such as transition dynamics and propagation of concentration shocks which yields important physical intuitions of the problem.

As depicted in Figure 3, we replace the concentration profiles given by eq 5 with uniform functions across the channel cross
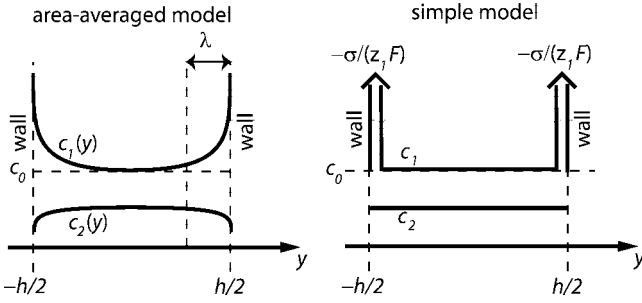
Figure 3. Wall normal distributions of the counterion, c_1, and the co-ion, c_2, in the area-averaged model and the simple model. The area-averaged model assumes Boltzmann distributions of ions in the wall normal direction, and these are determined as functions of the local value of c_0 (the local Boltzmann distribution coefficient) and local wall surface charge density. The simple model assumes uniform wall normal concentrations in the bulk for both ions. These concentrations are net neutral ($z_1 c_1 + z_2 c_2 = 0$) and vary in x and t. The entire double layer is modeled as a delta distribution of counterions shielding the local wall charge.

section and model the electric double layers (EDLs) with charge delta functions at the wall,

$$c_1(x, y) = c_0(x) + \frac{-\sigma(x)}{z_1 F}(\delta(y + h(x)/2) + \delta(y - h(x)/2)),$$

$$c_2(x, y) = \frac{z_1}{-z_2}c_0(x) \quad (23)$$

Here c_0, is the ion concentration in the channel other than the concentration which shields the wall charge. We included all of the EDL charges as counterions consistent with the case of ζ much higher than the thermal voltage.[39] Furthermore, the electroosmotic velocity is assumed to have a uniform profile across the channel height with zero velocity at the wall. These assumptions lead to $f = f^e = f_1^e = f_2^e = f_1^p = f_2^p = 1$. Therefore, from eq 22, E is given by

$$E = \frac{I}{Fz_1[F(z_1\nu_1 - z_2\nu_2)hc_0 - 2\nu_1\sigma]} \quad (24)$$

Equation 15 then reduces to

$$\frac{\partial}{\partial t}(hc_0) + \frac{\partial}{\partial x}\left\{Qc_0 + \frac{2\nu_1\nu_2z_2\sigma I}{Fz_1(\nu_1z_1 - \nu_2z_2)[F(z_1\nu_1 - z_2\nu_2)hc_0 - 2\nu_1\sigma]}\right\} = \frac{\partial}{\partial x}\left[hD_2\frac{\partial c_0}{\partial x}\right] \quad (25)$$

and Q will be (assuming zero pressure difference between the ends)

$$Q = -\int_{x_1}^{x_2}\frac{\varepsilon\zeta E}{\eta h^2}\,dx \bigg/ \int_{x_1}^{x_2}\frac{1}{h^3}\,dx \quad (26)$$

We can further simplify these equations by nondimensionalization. Assuming a constant wall charge and a reference length, h_{ref}, eq 25 can be nondimensionalized as follows:

$$\frac{\partial}{\partial t^*}(h^*c^*) + \frac{\partial}{\partial x^*}\left(c^* + \frac{I^*}{h^*c^*+1}\right) = \frac{1}{Pe}\frac{\partial}{\partial x^*}\left(h^*\frac{\partial}{\partial x^*}c^*\right) \quad (27)$$

where

$$t^* = \frac{tQ}{h_{ref}^2}, \quad x^* = \frac{x}{h_{ref}}, \quad h^* = \frac{h}{h_{ref}}, \quad \frac{1}{Pe} = \frac{D_2}{Q} \quad (28)$$

A convenient choice for h_{ref} is the typical Debye length in the problem or the length scale $-\sigma/(Fc_{ref})$.[40] With either choice, h^* is of order unity for a nanochannel and is much higher than unity for microchannels. c^* and I^* are defined as

$$c^* = \left(\frac{\nu_1 z_1 - \nu_2 z_2}{2\nu_1 z_1}\right)\frac{Fz_1 h_{ref}c_0}{-\sigma}, \quad I^* = \left(\frac{\nu_2 z_2}{2\nu_1 z_1}\right)\frac{Ih_{ref}}{\sigma Q} \quad (29)$$

$c^* h^*$ is the ratio of the bulk conductivity to the EDL conductivity (a local inverse Dukhin number[42]). A physical interpretation of I^* is a bit complicated and requires further analysis. Using eq 24, we see that

$$I^* h^* = \left(\frac{-u_2^{\text{electrophoretic}}}{u^{\text{bulk}}}\right)\left(\frac{\text{total conductivity}}{\text{EDL conductivity}}\right)$$

Therefore, $I^* h^*$ is a product of the coion electrophoretic-to-bulk velocity ratio and the total-to-EDL conductivity ratio. Respectively, these factors are measures of the importance of electromigration relative to bulk flow and the importance of electrolyte conductivity relative to that of EDL ions. Note that I^* is positive and if there is zero pressure difference between the ends of the channel, I^* can be computed from the nondimensional version of eq 26.

$$I^* = \int_{x_1^*}^{x_2^*}\frac{dx^*}{h^{*3}} \bigg/ \int_{x_1^*}^{x_2^*}\frac{dx^*}{\nu_2^* h^{*2}(c^* h^* + 1)},$$

$$\nu_2^* = \frac{\nu_2 z_2 F\eta}{\varepsilon\zeta} = \left(\frac{u_2^{\text{electrophoretic}}}{-u^{\text{electroosmotic}}}\right) \quad (30)$$

There are essentially four nondimensional parameters which describe the system: c^*, ν_2^*, Pe, and the profile of h^*. In this section, we assume that $PeL/h \gg 1$ (L is channel length) and thus Pe effects are assumed to be confined to a small vicinity of channel interfaces and concentration jumps (shocks). We later revisit this assumption and examine cases with small PeL/h values. In the latter case, we will show that molecular diffusion causes axial boundary layers to form at channel interfaces and whose axial length is proportional to PeL/h. For now (consistent with the experiments of Part II), we assume that channel lengths are much longer than these boundary layers.

Equations 27 and 30 are the simplest description for ion transport in variable height channels and are the focus of this study. Note these equations are obtained by combining all conservation principles (mass, momentum, species, and electric flux). Equation 27 has the form of a standard convection diffusion equation with an additional nonlinear flux term, $I^*/(h^*c^*+1)$. This term becomes important as the Debye length approaches within about an order of magnitude of channel height.

Characteristic Velocity and Shock Velocity. Equation 27 can be rearranged in the following form:

(38) Batchelor, G. K. *An Introduction to Fluid Dynamics*, 1st ed.; Cambridge University Press: Cambridge, UK, 1973.
(39) Hunter, R. J. *Zeta Potential in Colloid Science*; Academic Press: London, 1981.
(40) The nondimensional parameter $-2\sigma/(Fc_{ref}h)$ was proposed by Tessier and Slater[41] in the context of analyzing thick EDL problems in a closed channel. It describes the ratio of surface charge density to the number density of bulk ions.
(41) Tessier, F.; Slater, G. W. *Electrophoresis* **2006**, *27*, 686–693.
(42) Lyklema, J. *Fundamentals of Interface and Colloid Science*; Academic Press: London, 1995.
(43) Miller, P. D. *Applied Asymptotic Analysis*; AMS Bookstore: Providence, RI, 2006.

$$\frac{\partial}{\partial t^*}(h^* c^*) + \left(1 - \frac{h^* I^*}{(h^* c^* + 1)^2}\right)\frac{\partial c^*}{\partial x^*} = \left(\frac{c^* I^*}{(h^* c^* + 1)^2}\right)\frac{dh^*}{dx^*} + \frac{1}{Pe}\frac{\partial}{\partial x^*}\left(h^* \frac{\partial}{\partial x^*}c^*\right) \quad (31)$$

The coefficient of the convective term, $1 - h^* I^*/(h^* c^* + 1)^2$, is the velocity at which characteristics of c^* travel (nondimensionalized by the local bulk velocity).

$$U^* = 1 - \frac{h^* I^*}{(h^* c^* + 1)^2} \quad (32)$$

The characteristic velocity is the instantaneous, local velocity at which values of c^* travel in the system.[43] The sign of U^* determines the direction of travel of perturbations (information) in the system. Figure 4 shows how this characteristic velocity varies with concentration for a typical microchannel and nanochannel. Characteristic velocity is a monotonically increasing function of concentration which asymptotes to unity at very high concentration. However, for moderate concentrations, negative nanochannel U^* is possible while microchannels are still in their asymptotic, $U^* = 1$, limit (see Figure 4). We will see that this sign difference plays an important role in the propagation of CP concentration shocks. We say a channel is at the critical condition if its characteristic velocity is zero ($U^* = 0$). Correspondingly, we term positive U^* channels supercritical and negative U^* channels subcritical. Table 2 provides a summary of the terminologies that we here use to describe various conditions and properties. Some of these terminologies are introduced in the following sections of the paper.

The nonlinearity of eq 27 allows for development of concentration shock waves. We first analyze the propagation of

Table 2. Summary of Terminologies

terminology	description
characteristic velocity (U^*)	axial velocity at which concentration perturbations travel
critical condition	$U^* = 0$
supercritical condition	$U^* > 0$
subcritical condition	$U^* < 0$
propagation	term used for CP zones which expand (i.e., are not stationary); used to describe the motion of enrichment and depletion interfaces
shock velocity (V^*)	axial velocity at which concentration jumps travel; propagation rate
weak shock	shock between two regions with approximately equal characteristic velocities; characterizes enrichment-to-undisturbed interface.
strong shock	shock between two regions with significantly different characteristic velocities; characterizes depletion-to-undisturbed interface.
PeL/h	ratio of axial diffusion time to axial convection time; determines the portion of the channel length occupied by the extent of axial diffuse boundary layers.

a shock in a constant height channel. Figure 5 shows a schematic representation of a shock which travels with velocity V. The concentrations upstream and downstream of the shock are, respectively, c_u^* and c_d^*. In a coordinate system traveling with the shock, eq 27 will be

$$\frac{\partial}{\partial x^*}\left((1 - V^*)c^* + \frac{I^*}{h^* c^* + 1}\right) = \frac{1}{Pe}\frac{\partial}{\partial x^*}\left(h^* \frac{\partial}{\partial x^*}c^*\right) \quad (33)$$

The accumulation term vanishes, since the system is steady in the moving frame. The diffusion term is small far from the shock so that, by integrating eq 33 from far upstream to far downstream of the shock, we obtain the following relationship between c_u^*, c_d^*, and V^*:

$$(1 - V^*)c_u^* + \frac{I^*}{h^* c_u^* + 1} = (1 - V^*)c_d^* + \frac{I^*}{h^* c_d^* + 1} \quad (34)$$

For a shock to occur, the two characteristics (upstream and downstream of shock) should collide with each other. Characteristics, shown as arrows at the bottom of Figure 5, represent lines of constant concentration plotted in a x versus t plot. In such shocks, U_u^* is higher than U_d^* (otherwise, there is an expansion wave). Therefore, a necessary condition for the existence of a shock is $c_u^* > c_d^*$ (see Figure 4 and top of Figure 5). A larger difference between the characteristic velocities causes a stronger and thinner shock.

For a microchannel (large h^*), eq 34 can be further simplified. We consider two cases. In the first case, neither c_u^* nor c_d^* are small. Under such a condition, both U_u^* and U_d^* have nearly equal values close to unity (see Figure 4), and eq 34 reduces to $V^* \approx 1$. In other words, the shock will propagate with the speed of the bulk flow and the flow will experience a *weak* shock. As we shall see, weak shocks can occur in CP enrichment zones. In the second case, c_u^* is of order unity and c_d^* is much smaller than unity. Therefore, U_d^* can be negative and we will have a *strong* shock. In this case, eq 34 simplifies to

$$V^* = 1 - \frac{I^*}{c_u^*(h^* c_d^* + 1)} \quad (35)$$

If the downstream concentration becomes sufficiently small, a shock can move upstream through the microchannel. As we shall see, strong shocks can occur in CP depletion zones.
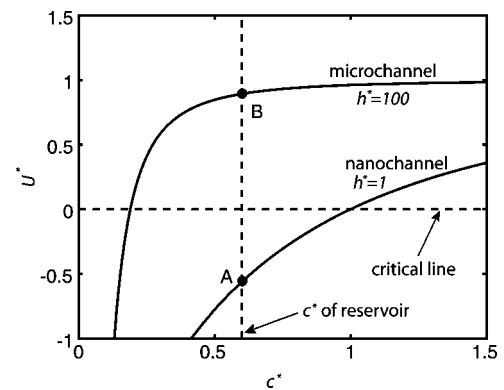

Figure 4. Nondimensional characteristic velocity versus nondimensional local concentration for a microchannel ($h^* = 100$) and a nanochannel ($h^* = 1$) (both for $I^* = 4$). c^* can be interpreted as an inverse Dukhin number based on a reference length (h_{ref}), while U^* is nondimensionalized by local bulk velocity. One possible c^* value based on a typical reservoir concentration is indicated. For this case, the microchannel has positive characteristic velocity (supercritical) and the nanochannel has negative characteristic velocity (subcritical).
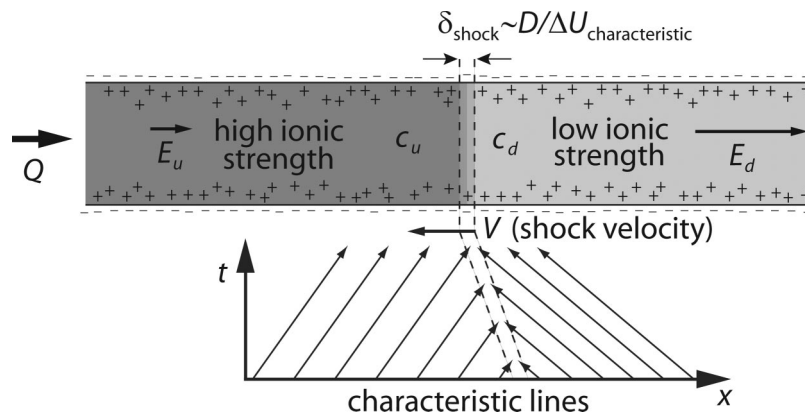
Figure 5. Illustration of concentration shocks in a microchannel. The region upstream of the shock has higher concentration than the region downstream. Consequently, the region upstream has higher characteristic velocity (see Figure 4). The shock thickness is governed by a balance between diffusion and change in characteristic velocity across the shock. The shock velocity can be either positive or negative and can be determined by a control volume analysis around the shock.

Nanochannel in Series with Two Microchannels. In this section, we consider a simple geometry to study the coupling between CP and bulk flow. Figure 6 shows a nanochannel in series with two microchannels, subdivided into five regions as follows: region 1 is the anode side microchannel, 2 is the converging zone, 3 is the nanochannel, 4 is the diverging region, and 5 is the cathode side microchannel. This configuration will be examined further through computations and experiments in Part II. As we shall discuss, CP always occurs to some degree in this configuration, while propagation may or may not occur. Understanding of the regimes and dynamics associated with CP propagation in this geometry is an essential step to understanding more complex geometries, for example, with micro- and nanochannels arranged in series and parallel.

We assume the nanochannel hydraulic resistance is much higher than that of the microchannel so that $l_{nano}/h^3_{nano} \gg l_{micro}/h^3_{micro}$. Furthermore, in the high PeL/h limit (we will examine axial diffusion effects later), we assume that concentration and ζ are nearly uniform through the nanochannel but can vary with time. Therefore, eq 30 can be approximated by

$$I^* = \frac{v^*_{2n}}{h^*_n}(c^*_n h^*_n + 1) \tag{36}$$

where the subscript n represents the nanochannel (region 3).

Startup and Transient Dynamics. In this section, we first describe one scenario in which CP enrichment and depletion zones propagate to the cathode and anode sides, respectively. We then extend this scenario to other cases and obtain a general criterion to predict whether CP zones propagate.

We use eq 31 to describe the evolution of the system. Prior to the application of an external electric field, all sections of the channel are in equilibrium with end-channel reservoirs and thus c^* is uniform and equal to the reservoir concentration, c^*_r. Immediately after current is applied, the first term in the right-hand side of eq 31 (proportional to dh/dx) will cause local enrichment in region 4 and local depletion in region 2 (see Figure 6). These depletion and enrichment regions will convect in the channel in a direction governed by the local characteristic velocity. In this particular scenario, as shown in Figure 6 (and Figure 4), we assume that the initial characteristic velocity is negative in the nanochannel (and positive in microchannels). The characteristic velocities transport perturbations away from region 4 in

both directions into regions 3 and 5. In contrast, the depletion in region 2 will not penetrate into neighboring regions because the characteristic velocities are locally inward. This means the concentration in region 2 will decrease until c^* reaches small values. The latter effect decreases the characteristic velocity (see Figure 4).

Eventually, a sufficiently low concentration is reached in region 2, so that according to eq 35 a shock with negative velocity will form between regions 1 and 2. This shock propagates upstream through the entire length of the microchannel, so that region 1 will eventually become subcritical. On the cathode side of the nanochannel, CP enrichment will propagate from region 4 into the nanochannel (region 3) and act to increase the concentration of the nanochannel. This will increase U^* within the nanochannel (see Figures 6 and 4). This increase of ion concentration proceeds until the nanochannel reaches the critical condition. At this point, the accumulation zone ceases to penetrate into the nanochannel and the nanochannel reaches the steady state condition. Meanwhile, an accumulation shock will propagate forward in region 5. Together, these details help estab-
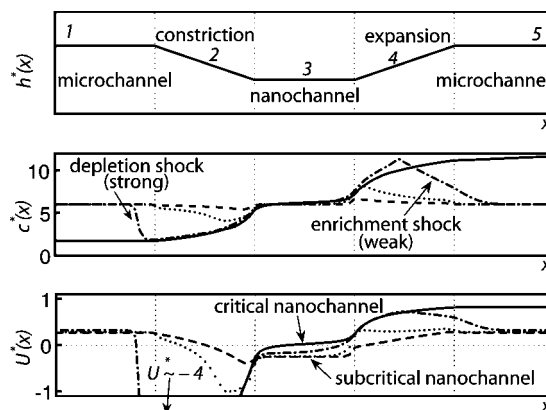

Figure 6. Top: Channel height profile in the microchannel–nanochannel–microchannel system studied here. Five regions are identified in the channel. Regions 1, 3, and 5 have constant areas. Area-averaged concentration profiles (center) and characteristic velocity profiles (bottom) for various times are shown. Shown is a case where CP propagates where $t^* = 1$ (dashed line), $t^* = 4$ (dotted line), $t^* = 16$ (dash-dotted line), and $t^* = 64$ (solid line). Note that an initial negative characteristic velocity in the nanochannel blocks the penetration of the depletion zone into region 3 and allows for advancement of the enrichment zone into this region. This slightly increases the nanochannel concentration until its characteristic velocity reaches zero.

(44) Saad, M. A. *Compressible Fluid Flow*, 2nd ed.; Prentice Hall: Upper Saddle River, NJ, 1992.

lish the steady state ion concentrations throughout the whole system.

Global steady state will be achieved when the depletion shock and enrichment shock leave the microchannels. At that point, the depletion zone microchannel will be in a subcritical condition, the nanochannel will be at the critical condition, and the enrichment zone microchannel will be in a supercritical condition. This situation is somewhat analogous to steady compressible flow through converging−diverging nozzles in which the converging section is subsonic, the throat is sonic, and the diverging section is supersonic.[44]

In micro-nanochannels, the sign of the characteristic velocity is critical in causing propagation of CP zones. As a simple rule, negative U^* (in the nanochannel or at the anode side interface) triggers propagation of CP zones. Another interesting observation is that if CP propagates, the nanochannel always achieves a unique ion concentration which is independent of the initial ion concentrations in the system (!) and which can be determined by applying the critical condition ($U^* = 0$) in the nanochannel. Physically, this important result means that nanochannel concentrations are not determined by "the user," but are instead governed by the effect of the surface chemistry which causes surface charge density and drives the development of the problem. The assertion that an experimentalist can always arbitrarily vary and control steady state ion density in nanochannel systems (as has been assumed by all studies to date[4,5,7,9,14,16,18,21,45]) is therefore incorrect.

On the Conditions for the Propagation of CP. In the previous section, we observed that if a nanochannel is initially at subcritical condition, CP propagates. However, this is not the only case in which propagation occurs, and, in general, the initial concentration of the reservoir (together with v_{2n}^*) determines if propagation may or may not occur. To extend the analysis, we assume the simplification given by eq 36 and rewrite eq 27.

$$\frac{\partial}{\partial t^*}(h^* c^*) + \frac{\partial}{\partial x^*}\left(c^* + \frac{(v_{2n}^*/h_n^*)(c_n^* h_n^* + 1)}{h^* c^* + 1}\right) = \frac{1}{Pe}\frac{\partial}{\partial x^*}\left(h^*\frac{\partial}{\partial x^*}c^*\right)$$
(37)

At steady state, the accumulation term in eq 37 vanishes and the sum of the nonlinear advective flux and the diffusive flux reach a constant value through the entire domain. Away from regions 2 and 4 (in Figure 6), diffusive flux is negligible and thus at steady state we will have the following condition:

$$(t \to \infty) \Rightarrow c_1^* + \frac{(v_{2n}^*/h_n^*)(c_n^* h_n^* + 1)}{h_1^* c_1^* + 1} = c_n^* + (v_{2n}^*/h_n^*)$$
$$= c_5^* + \frac{(v_{2n}^*/h_n^*)(c_n^* h_n^* + 1)}{h_5^* c_5^* + 1}$$
(38)

Given c_n^*, we can solve eq 38 for steady state values of c_1^* and c_5^*. We see that c_1^* and c_5^* each have two solutions (roots), one supercritical and one subcritical solution.[46] For c_5^*, only the supercritical solution is physical. A subcritical c_5^* is not allowed since the reservoir concentration entering region 5 would act to change the sign of U^* locally, creating a supercritical condition. The two roots of the steady solution for c_1^* are both possible; and physically these are selected by the initial condition. The

supercritical solution of c_1^* allows for anode reservoir information to convect into region 1 and thus makes its concentration the same as that of the reservoir. The subcritical solution allows for nanochannel information to travel toward the anode side reservoir (thus establishing channel ion densities determined by surface chemistry and ion mobility). These super- and subcritical conditions correspond to CP with no propagation and CP with propagation, respectively.

CP with No Propagation. Under this condition, characteristic lines originate at the upstream (anode) reservoir and extend throughout the field to the downstream (cathode) reservoir. The anode reservoir therefore determines the concentration at each section. This leads to the following steady state solution to eq 38 (assuming sufficiently large microchannel h^*):

$$c_1^* = c_5^* = c_r^*, \quad c_n^* = c_r^* - v_{2n}^*/h_n^*$$
(39)

Hence, using eqs 32 and 36, we obtain the following value for characteristic velocity in the nanochannel:

$$U_n^* = 1 - \frac{h_n^* I^*}{(h_n^* c_n^* + 1)^2} = 1 - \frac{v_{2n}^*}{(h_n^* c_r^* + 1 - v_{2n}^*)}$$
(40)

This solution is physically possible if eqs 39 and 40 yield positive values to both c_n^* and U_n^*. As a result, $c_r^* h_n^* > \max(v_{2n}^*, 2v_{2n}^* - 1)$ is the validity condition for this solution. This can be shown in a $c_r^* h_n^* - v_{2n}^*$ diagram as in Figure 7. The solid line shows the boundary over which CP without propagation is physically possible. As shown, for $v_{2n}^* > 1$, this boundary represents $U_n^*(t \to \infty) = 0$ (see eq 40). For $v_{2n}^* < 1$, it represents $c_n^*(t \to \infty) = 0$ (see eq 39). Correspondingly, we will have two different regimes where CP propagates.

CP with Propagation. As we noted earlier, negative (or zero) characteristic velocities are key to CP propagation. Based on this, we can identify two scenarios under which CP can propagate. In one scenario, the nanochannel reaches zero characteristic
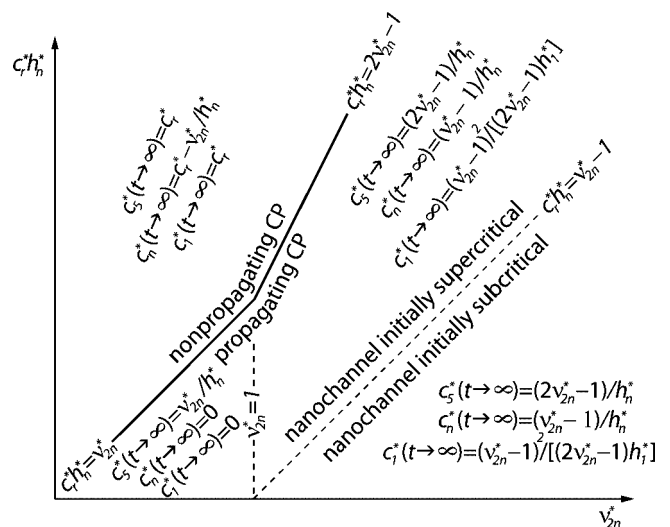

Figure 7. Regimes of CP in a nondimensional reservoir concentration (inverse Dukhin number for nanochannel) versus nondimensional co-ion mobility. The solid line represents the boundary between initial conditions which lead to propagating CP and nonpropagating CP. The propagating CP zone can be further divided into three regions indicated by dashed lines. In the first region (from right), the nanochannel's initial condition is subcritical (oblique dashed line). In the second region, the nanochannel is initially supercritical but reaches the critical condition at steady state. In the third region, the nanochannel always stays supercritical. The steady state solutions of the concentrations of regions 1, 3 (subscript "n"), and 5 of Figure 6 are shown.

(45) Burgreen, D.; Nakache, F. R. *J. Phys. Chem.* **1964**, *68*, 1084–1091.
(46) A quick proof would be as follows: Both of these c_5^* values result in the same flux and thus can be the c_u^* and c_d^* of a stationary shock. Therefore, the sign of their characteristic velocities should be different. Otherwise, the shock will not remain stationary and will move in the direction of the characteristic velocity.
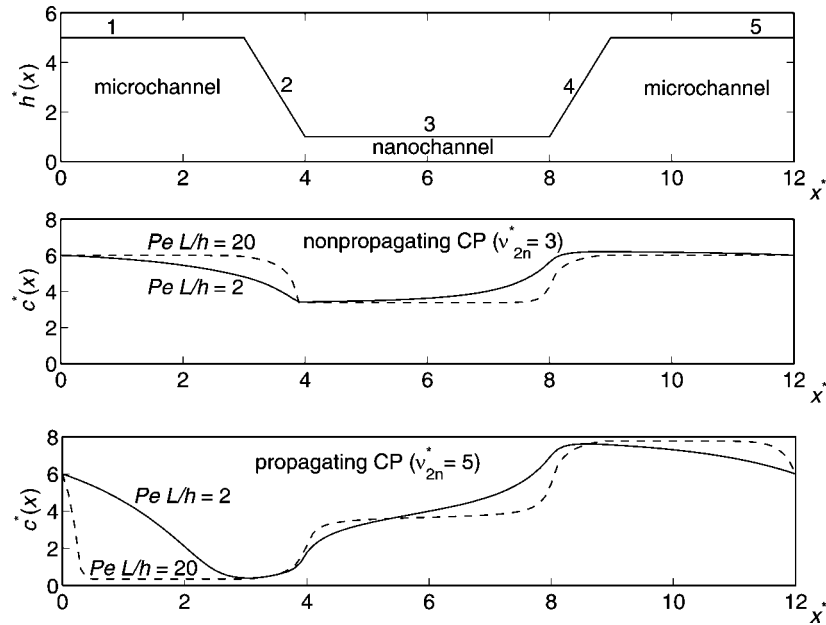
Figure 8. Effect of ion diffusion on the steady state shapes and axial extent of ion depletion and enrichment zones. In the nonpropagating case (center), the steady state values of concentrations are symmetric far from interfaces and for high *PeL/h* CP is negligible. In lower *PeL/h* regimes, diffusive flux causes local axial boundary layers which lead to nonsymmetric concentration profiles. This diffusive dominated polarization is interpreted as nonpropagating CP. In the propagating case (bottom), diffusion effects also cause axial boundary layers at the channel interfaces. Due to physical mismatch of microchannels' steady concentration with reservoir, additional boundary layers are observed at channel ends. At the low *PeL/h* limit, these boundary effects even extend to the nanochannel and limit the CP propagation length.

velocity, and in the other case region 2 becomes locally critical while the nanochannel remains supercritical.

If $v_{2n}^* > 1$, the nanochannel reaches a critical condition ($U_n^*(t \to \infty) = 0$) and the following will be the solution to eq 38:

$$c_n^* h_n^* = v_{2n}^* - 1, \quad c_5^* h_n^* = 2v_{2n}^* - 1, \quad c_1^* h_1^* = \frac{v_{2n}^{*2}}{(2v_{2n}^* - 1)} - 1 \tag{41}$$

Using this solution in eq 35, the depletion shock velocity will be

$$V_1^* = 1 - \frac{2v_{2n}^* - 1}{h_n^* c_r^*} \tag{42}$$

This solution is physically possible only for negative V_1^* (we need the shock to propagate toward the anode). This leads to $h_n^* c_r^* < 2v_{2n}^* - 1$ as the validity condition for this solution, which is the aforementioned boundary line in Figure 7. The fact that these two boundaries coincide confirms the uniqueness of the solution. In other words, for a given (initial) condition, only one of these solutions (propagating or nonpropagating CP) is physically possible.

If $v_{2n}^* < 1$, eq 41 will not provide a physical answer to the problem (it yields a negative concentration). The physical answer is

$$c_1^* = c_n^* = 0, \quad c_5^* h_n^* = v_{2n}^* \tag{43}$$

Using this solution, the depletion shock velocity will be

$$V_1^* = 1 - \frac{v_{2n}^*}{h_n^* c_r^*} \tag{44}$$

Note that if $v_{2n}^* < 1$, the nanochannel never reaches a critical condition and the transition to propagating CP is triggered when a location in region 2 reaches critical condition. Zero c^* in this

case implies that there will be no coion in the nanochannel and in regions 1 and 2. In this case, the model predicts that only EDL ions conduct the current (note we do not account for the dissociation of water molecules[27]).

Diffusion Effects. Lastly, we note the effects of diffusion in determining the spatial extent of CP zones in both propagating and nonpropagating cases. Figure 8 (top) shows a schematic of the series micro-, nano-, and microchannel studied here. The plots show steady state streamwise concentration profiles indicating the effect of an order magnitude change of *PeL/h* = 2, 20. For simplicity of presentation, we here study microchannels with axial lengths on the same order as the nanochannel length.

The plot in the middle of Figure 8 is for $v_{2n}^* = 3$, a case where at steady state $c_1^* \simeq c_5^* \simeq c_r^*$ and so propagation of shocks does not occur. For all values of *PeL/h*, axial molecular diffusion determines the extent of diffuse axial boundary layers at micro-to-nanochannel interfaces. For large *PeL/h*, these boundary layers are small and thus the steady state concentration in the microchannels is nearly symmetric and uniform; therefore, polarization is negligible. As *PeL/h* decreases, diffuse boundary layers at the micro-to-nanochannel interfaces grow axially, since diffusive fluxes act against local characteristic velocities. In this case, polarization can become significant with some polarization inside the nanochannel itself (i.e., a concentration increase which extends from the cathode side into the nanochannel) as shown in Figure 8 (middle).

The bottom plot of Figure 8 is for $v_{2n}^* = 5$, where CP propagates (subcritical c_1^* and supercritical c_5^*). In this case, while the underlying propagation is governed by characteristics, diffusion effects again result in axial boundary layers at interfaces. Since in this case the microchannel concentrations are different from that of the reservoir, two additional boundary layers are observed at the reservoir-to-microchannel interfaces. At high *PeL/h*, these boundary layers are confined to the interfaces and the steady state concentration profile is strongly polarized in the system,

and nearly uniform within each microchannel. As PeL/h decreases, these boundary layers grow. At low PeL/h, the two reservoir-to-microchannel boundary layers can extend to the nanochannel and influence and eventually overwhelm propagation effects. In the limit of very high diffusion fluxes (low PeL/h), the depletion shock will have an axial thickness of order channel length and "propagation" of CP might not be observable in a transient measurement. However, we still classify this case as propagating CP, since the underlying characteristics dictate outward propagation of these enrichment and depletion zones (albeit balanced by diffusion). In contrast to the nonpropagating case, axial diffusion tends to limit the extent of enrichment and depletion zones created by propagating CP.

We note Rubinstein and Zaltzman[29] and Rubinshtein et al.[47] analyzed concentration polarization across an ion exchange membrane and showed a "local" depletion zone adjacent to the membrane followed by a diffuse layer emerging from the reservoir. This is very similar to the depletion zone in the bottom plot of Figure 8 for the low PeL/h case. In an earlier analysis, Mishchuk and Takhistov[25] reported similar features for CP caused by ionic current into and around ionically conductive particles. Given their published parameters, we estimate that all of these experimental studies explored a regime which we here refer to as the "propagating CP", but at low PeL/h. As mentioned earlier, in such a regime, propagation of characteristic lines is indeed outward away from the nanochannel but the size of CP zones is reduced due to diffusion boundary layers which form at reservoir-to-channel interfaces. The result is enrichment and depletion regions which form, but whose maxima and minima, respectively, move negligibly and propagation dynamics are difficult to observe (compared to the high PeL/h regime). This in fact is a strong motivation for the current work as the high PeL/h regime is especially important for fluidic devices which integrate nanochannel sections into networks of, say, centimeter-long microchannels (and which operate with typical time scales of the order of 10 s and longer). We will examine such a system in Part II.

Conclusions

We developed two models for the analysis of concentration polarization at micro-nanochannel interfaces. Numerical solutions using the area-averaged model and its comparison to experiments will be given in Part II of this two-paper series. Here, we have shown that characteristic analysis yields significant insight into the dynamics of CP and development of depletion and enrichment zones. The analysis applied to the simple model identifies two CP regimes (with and without propagation). For negative wall charge, if CP propagates, the model predicts a region of high concentration which propagates from the cathode side nano-channel−microchannel interface into the cathode side micro-channel, and a region of very low concentration which propagates from the anode side interface into the anode side microchannel. In the regime without propagation, CP causes stationary regions of local high and low concentration at the cathode and anode side interfaces, respectively. Using characteristic analysis, the model describes the transient dynamics and steady state solutions for CP.

The following points (mostly summarized in Figure 7) are perhaps the most interesting results of the current analysis of a nanochannel positioned between two microchannels:

  1 In this system with a nanochannel between two micro-channels, some amount of CP will always occur, but CP

may or may not propagate. If PeL/h is large and CP does not propagate, then polarization effects are negligible.

  2 The important parameters determining whether CP propa-gates are $h_n^* c_r^*$ (a nanochannel inverse Dukhin number based on reservoir concentration) and v_{2n}^* (ratio of electrophoretic velocity of coions to electroosmotic velocity). Other parameters such as microchannel dimensions, magnitude of applied current, axial diffusion, and so forth do not play a role in determining propagation. CP may occur even if double layers do not overlap.

  3 If CP does not propagate, the steady state ion concentration in the nanochannel is determined by the reservoir ion concentration c_r^* and the nanochannel properties via v_{2n}^*/h_n^*, as shown in Figure 7. Here, axial diffusion governs the extent of diffuse boundary layers at the micro-to-nanochan-nel interfaces. As PeL/h decreases from high values, polarization regions become observable and extend over longer distances into the channel. The nanochannel itself becomes polarized.

  4 If CP propagates, the steady state ion concentrations in the nanochannel and microchannels fall into three regimes as shown in Figure 7. For large PeL/h, the final ion concentra-tion in each channel section (in all three regimes) is nearly uniform and independent of the initial condition. These concentrations are determined by surface chemistry, nanochannel height, microchannel height, and ion mobility (via v_{2n}^*, h_n^*, and h_1^*). Under such a condition, characteristics of c^* will emerge from the nanochannel toward the end boundaries and thus information (perturbations) cannot propagate into the system from the reservoir (e.g., so that the final nanochannel ion density is independent of the initial value in the reservoir!). In cases where CP propagates, diffusion effects cause axial boundary layers at channel and reservoir interfaces. For low values of PeL/h, gradients associated with these boundary layers can penetrate throughout the entire channel system, and so the extent of propagation of CP is suppressed by diffusive effects.

  5 As a rule of thumb, propagating CP occurs for large $v_{2n}^*/(h_n^* c_r^*)$. This can be explained intuitively. For large concentrations, current carried by the EDLs becomes negligible and the composite channel system behaves like a typical microchannel. Thus, even CP becomes negligible. On the other hand, to create propagating CP and achieve a subcritical condition in the anode side microchannel, the system needs to transmit information upstream and that is only possible with negative ions of high enough mobility.

Appendix A: Two-Dimensional (2D) Reconstruction of Area-Averaged Model Solutions

Figure A1 shows an example solution of recirculation regions (in flow velocity) resulting from internal pressure gradients induced by electrokinetic flow at an interface between a microchannel and a nanochannel. To obtain this, we first solve for the axial profile of the quantity c_0 using the area-averaged model. The solution for $c_0(x,t)$ yields the area-averaged pressure-driven flow, $\overline{u^p}$, and the electroosmotic Helmholtz−Smo-

　(47) Rubinshtein, I.; Zaltzman, B.; Pretz, J.; Linder, C. *Russ. J. Electrochem.* **2002**, *38*, 853−863.
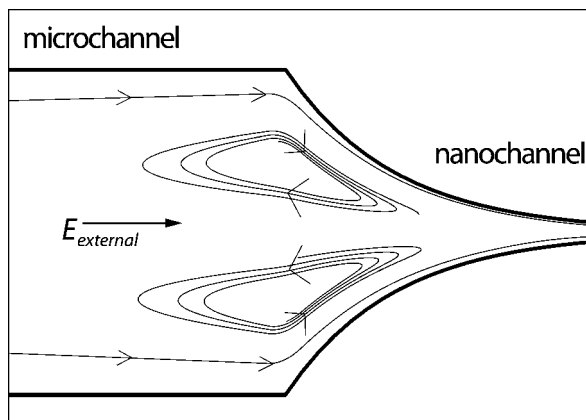
Figure A1. Example prediction of recirculation vortices resulting from our area-averaged model in a 2D (infinite width) channel. The micro-to-nanochannel height is arbitrarily taken to vary exponentially from 1 μm to 50 nm. We assume surface charge densities of -0.0062 C/m^2 for the microchannel and -0.0043 C/m^2 for the nanochannel with smooth variation at the interface. The applied current density is 4×10^{-5} A/m. Other parameters include the nominal concentration ($c_r = 1$ mM), binary buffer valences of 1 and -2, and respective diffusivities of 1.5×10^{-9} and 5.4×10^{-10} m^2/s.

luchowski velocity, u_0^e (see the solution method to the area-averaged model). Further, consistent with the model assumptions, at each axial location, the parallel parabolic velocity profile is used to reconstruct the axial component of the 2D pressure-driven velocity. The 2D electroosmotic velocity field is reconstructed using solution of the Poisson–Boltzmann equation ($u^e(y) = u_0^e(1 - \psi^*/\zeta^*)$). The vertical component of the velocity field is obtained by integrating the local continuity equation at each axial location. The figure shows the velocity field streamlines obtained from this reconstruction. As shown, two-dimensional vortex structures are captured fairly well by the model and the streamlines exhibit the impenetrable wall constraint (the no slip condition is automatically satisfied by the reconstruction). We hope to further study the creation and influence of these vortices on the flow in a future paper. These recirculations are a result of the difference in flow rate per current between the nano- and microchannel sections. For now, we note the 2D predictions are consistent with the work of Park et al.[18] and Postler et al.[31] who also observed recirculation regions in similar flow fields.